Improved fractional-order hysteresis-equivalent circuit modeling for the online adaptive high-precision state of charge prediction of urban-electric-bus lithium-ion batteries.

ZENG, J., WANG, S., CAO, W., ZHANG, M., FERNANDEZ, C. and GUERRERO, J.M.

2024

Improved fractional-order hysteresis-equivalent circuit modeling for the online adaptive high-precision state of charge prediction of urban-electric-bus lithium-ion batteries

Jiawei Zeng[a], Shunli Wang[a*], Wen Cao[a], Mengyun Zhang[a], Carlos Fernandez[b], Josep M. Guerrero[c]

([a] *School of Information Engineering, Southwest University of Science and Technology, Mianyang 621010, China*

[b] *School of Pharmacy and Life Sciences, Robert Gordon University, Aberdeen AB10-7GJ, UK*

[c] *Department of Energy Technology, Aalborg University, Pontoppidanstraede 111 9220 Aalborg East, Denmark)*

Abstract: Accurate state of charge (SOC) estimation is based on a precise battery model and is the focus of the battery management system (BMS). First, based on the second-order RC equivalent circuit model and Grunwald-Letnikov (G-L) definition, the high-precision fractional-order hysteresis-equivalent circuit model (FH-ECM) is established considering the open-circuit voltage hysteresis effect. Then, the global parameters of the battery model are identified using a particle swarm algorithm optimized by the genetic algorithm (GA-PSO). Thirdly, a fractional-order adaptive unscented Kalman filter (FOAUKF) algorithm is derived to estimate the SOC of lithium-ion batteries. Finally, the feasibility of the model and algorithm is verified under complex working conditions. Under the dynamic stress test (DST) condition, the accuracy of model terminal voltage has been improved by 37.83%, and the error of SOC estimation has been reduced by 11.28%. Under Beijing bus dynamic stress test (BBDST) condition, the model terminal voltage accuracy has been improved by 51.44%, and the SOC estimation error has been reduced by 35.71%. The experimental results fully confirm the accuracy of the fractional-order hysteresis equivalent circuit modelling method.

Keywords: *Lithium-ion batteries; Fractional-order hysteresis model; GA-PSO algorithm; fractional-order adaptive unscented Kalman filter; Beijing bus dynamic stress test;*

Corresponding author: *Shunli Wang. Tel/fax: +86-15884655563. E-mail address: wangshunli@swust.edu.cn.*

1. Introduction

New energy vehicles have been pushed onto the stage of history due to factors such as the energy crisis and environmental pollution [1]. Compared to conventional fuel vehicles, new energy vehicles must solve the technical problems linked to batteries [2, 3]. The accurate battery model is the premise of SOC estimation and the basis of the battery management system (BMS) [4, 5]. Obtaining an accurate battery model and simulating the actual characteristics of batteries is a challenge in practical application. The highly non-linear nature of battery systems, the complexity of internal chemical reactions, and the variety of application scenarios increase the difficulty of modelling batteries [6]. In addition, battery status estimation is affected by historical status, which makes it challenging to build a model with memory characteristics.

To simulate the process and behaviour of batteries, the models mainly include the electrochemical model, the data-driven model, and the equivalent circuit model (ECM) [7-10]. ECM is the best model for BMS, considering model accuracy and complexity. ECM includes the Thevenin model, the partnership for a new generation of vehicles (PNGV)

model, and the second-order RC model. The Thevenin model has a simple structure and high accuracy and is widely used in practice [11]. The partnership for a new generation of vehicles (PNGV) model has higher estimation accuracy, but parameter identification is more complex [12]. There are many algorithms for estimating SOC based on ECM [13]. Fu et al. [14] used the weighted multi-innovation cubature Kalman filter (KF) method to estimate SOC based on the Thevenin model, which improved the accuracy significantly. Ref. [15] Considering the effects of temperature and C-rates based on the Thevenin model and the SOC of lithium batteries was estimated using the unscented Kalman filter (UKF). Chen et al. [16] proposed an improved H -infinity method based on historical data of the battery, which has a high accuracy of SOC estimation based on the one-order RC model. In addition, with the increasing computing power of the BMS, some new models and methods have been proposed. Yang et al. [17] used a long and short-term memory network to learn and reduce the effects of temperature changes in the battery, with high accuracy in SOC estimation at different temperatures. Shi et al. [18] established an adaptive multi-timescale ECM based on the second-order RC model to analyze the fast and slow change of parameters in each region, which has higher accuracy and practicality. Ref. [19] comprehensively considered the effects of the state of health (SOH), SOC, and temperature and established a comprehensive equivalent circuit mode. Ref. [20] proposed a new modelling method using the Wiener structure based on ECM and derived a parameter identification algorithm for the model. Hu et al. [21] proposed a joint estimation strategy for SOC and SOH using dual particle filtering based on the second-order RC model. Wang et al. [22] proposed a modelling method of feedforward long short-term memory to estimate the entire cycle SOC considering the influence of temperature. However, Ref. [14-16] overlook the influence of the open circuit voltage (OCV) hysteresis effect, and the maximum error of OCV caused by the hysteresis effect exceeds 0.1V. Shi et al. [18] analyzed the voltage hysteresis effect and obtained higher model accuracy. Ref. [23] established a first-order RC model considering the hysteresis effect for SOC estimation, and its verification results show that the model considering the hysteresis effect has better estimation accuracy and rate of convergence.

However, the above methods use integer-order models. If the model's structure differs from the characteristics performed by the cell, the perfect parameter identification algorithm is also difficult to break through the structural constraints. Studies have shown that many natural manifolds have fractional-order properties [24-26]. The application of fractional-order systems in battery models has received attention, mainly by introducing Constant Phase Element (CPE) to establish a fractional-order model (FOM) and algorithms to estimate the state of batteries [27-29]. Ref. [30] analyzed the terminal voltage estimation results of FOM and integer-order models and concluded that FOM has higher estimation accuracy. Guo et al.[31] analyzed lithium-ion batteries' solid-state diffusion mechanism and established a clear physical significance FOM. Wang et al. [32] proposed a fractional-order model for the supercapacitor and used a particle swarm optimization algorithm of chaos theory for parameter identification. After experimental analysis, it was concluded that FOM is more reasonable and applicable. In addition, the electrochemical impedance spectrum of lithium-ion batteries also exhibits fractional-order characteristics [33]. With the maturity of fractional order technology, some improved

FOMs have been proposed. Reference [34] established a FOM considering the influence of temperature on parameters, which enhances the estimation accuracy and stability of the model. Reference [35] proposes partially adaptive FOM based on different time scales with higher SOC estimation accuracy under different working conditions. Similarly, the KF algorithm can be applied to FOM. Ref. [36] analyzed the SOC estimation results of different fractional-order extended Kalman filtering (FOEKF) algorithms based on FOM. The results showed that FOEKF had better accuracy than EKF. Ref. [37] proposed an improved fractional-order KF method for SOC estimation; the root mean squared error (RMSE) is 0.19% under Urban Dynamometer Driving Schedule (UDDS) test. However, for the highly non-linear system of power batteries, the EKF ignores high-order information during Taylor expansion, which may cause linearization errors and system instability. Therefore, optimizing existing models and developing advanced SOC estimation algorithms are significant.

The computational complexity of fractional-order differentiation makes FOM modelling more difficult than the integer-order model. It is crucial to accurately identify the parameters of the FOM and develop a state estimation algorithm based on the FOM. The FOM in Ref. [34,35] does not consider the battery's hysteresis effect and the inconsistency of the resistance in the charging or discharging state. To solve the modelling and SOC estimation of the battery, the main contributions of this paper are as follows: (i) the CPE is introduced based on the second-order RC equivalent circuit model, and considering the open-circuit voltage hysteresis effect, the high precision fractional-order hysteresis - equivalent circuit model (FH-ECM) is established; (ii) The global parameters of the model were identified using the genetic algorithm optimized particle swarm algorithm (GA-PSO); (iii) The state space equations of FH-ECM are derived and proposed the SOC estimation strategy based on the fractional-order adaptive unscented Kalman filter (FOAUKF); (iv) The feasibility of FH-ECM and FOAUKF was verified by comparing the experimental results of the second-order RC model and FOM.

This work established a high-precision FH-ECM based on the model structure, and the proposed FOAUKF algorithm has high SOC estimation performance. The remaining content of this paper is as follows: Section 2 proposes FH-ECM based on battery characteristics and proposed GA-PSO algorithm FOAUKF algorithm for parameter identification and SOC estimation. Section 3 conducted experimental verification of the model and algorithm in Section 2. Section 4 is the Conclusion.

2. Theoretical analysis

2.1. Fractional-order hysteresis equivalent circuit modeling

Most capacitors have fractional-order characteristics, and fractional capacitance in the frequency domain is defined as shown in Eq. (1), C is the capacitance value, and n is the order of the capacitance, $0 < n < 1$. The battery model only introduces fractional differentiation and does not involve integration. The definition of Grunwald-Letnikov simplifies derivative calculations and is more applicable to discrete systems, as shown in Eq. (2).

$$\mathbb{Z}(\mathrm{j}\varpi)=\frac{1}{\mathrm{C}(\mathrm{j}\varpi)^{\mathrm{n}}} \tag{1}$$

$$\begin{cases} d^{\alpha}f(x)=\lim\limits_{T\to 0}\dfrac{1}{T^{\alpha}}\sum\limits_{m=0}^{L}(-1)^{m}\binom{n}{m}f(x-mT) \\ \binom{n}{m}=\dfrac{n!}{m!(n-m)!} \end{cases} \tag{2}$$

d^{α} is the fractional-order differential operator, α is the order of the system, T is the sampling time of the system, and L is the memory length. The result of the dispersion of Eq. (2) can be obtained as shown in Eq. (3).

$$\begin{cases} d^{\alpha}x_k=\dfrac{1}{T^{\alpha}}\sum\limits_{j=0}^{k}(-1)^{j}\binom{\alpha}{j}x_{k-j} \\ \binom{\alpha}{j}=\begin{cases} 1 & j=0 \\ \dfrac{\alpha(\alpha-1)\cdots[\alpha-(j-1)]}{j!} & j>0 \end{cases} \end{cases} \tag{3}$$

$\binom{\alpha}{j}$ is the Newton binomial coefficient, k is the current sampling time. Eq. (3) shows that the current state of fractional-order systems relates to the historical state.

Systems with a long memory, dynamic diffusion, and retardation effects can be optimized by introducing fractional derivatives, such as the material migration process and the double-layer effect of batteries [38, 39]. The electrochemical impedance spectra of lithium-ion batteries show fractional-order characteristics. In the mid-frequency region of electrochemical impedance spectroscopy (EIS), the battery impedance is shown as a semi-ellipse, as shown in Fig. 1, which is related to the charge transfer effect at the electrolyte interface and the double layer effect.

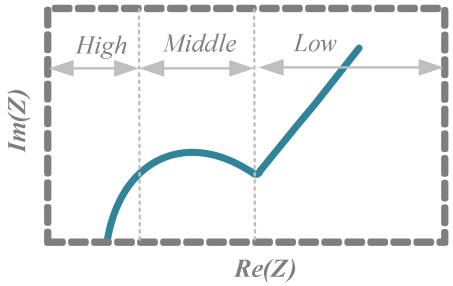

Fig.1. The electrochemical impedance spectra of lithium-ion batteries

The RC network of the standard integer-order ECM is shown as a perfect semicircle in the impedance spectrum, which differs from the oval shape of the battery. By increasing the number of RC networks, the actual performance of batteries can be approached gradually. However, the difficulty of parameter identification and the computational burden of BMS is significantly increased. Based on the second-order RC equivalent circuit model and considering the effect of delay voltage, an improved fractional equivalent circuit model is established by introducing CPE, as shown in Fig. 2.

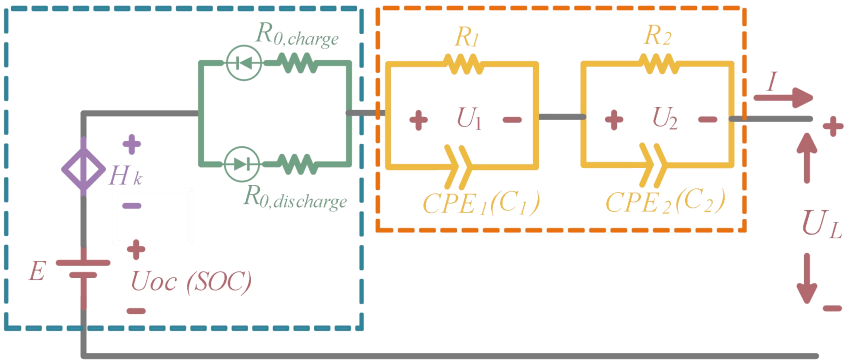

Fig.2. The fractional-order hysteresis - equivalent circuit model (FH-ECM) of lithium-ion batteries

U_{OC} is the open-circuit voltage, $R_{0,charge}$ and $R_{0,discharge}$ represents the ohm internal resistance in charge and discharge, R_1 and R_2 represents the charge transfer internal resistance and diffusion internal resistance. U_1 is the voltage of the CPE_1, α is the order of the CPE_1; U_2 is the voltage of the CPE_2, β is the order of the CPE_2. CPE has characteristics between capacitance and resistance, when $\alpha = \beta = 1$, CPE is equivalent to the ideal capacitance; when $\alpha = \beta = 0$, CPE is equivalent to the ideal resistance. According to the circuit principle, the following can be obtained:

$$\begin{cases} U_L = U_{OC} + H_k - I_L R_0 - U_1 - U_2 \\ d^{\alpha}U_1 = \dfrac{I_L}{C_1} - \dfrac{U_1}{R_1 C_1} \\ d^{\beta}U_2 = \dfrac{I_L}{C_2} - \dfrac{U_2}{R_2 C_2} \end{cases} \tag{4}$$

H_k is the hysteresis voltage used to reflect the hysteresis effect of the battery [40], which can be expressed as:

$$H_{k+1} = e^{\left(-\left|\frac{\eta I(k)\gamma T}{Q_N}\right|\right)} H_k + \left[1 - e^{\left(-\left|\frac{\eta I(k)\gamma T}{Q_N}\right|\right)}\right] M(H) \tag{5}$$

γ is a hysteresis decay rate constant, a positive constant used to regulate the decay rate. $M(H)$ is the maximum hysteresis; the OCV calculates it during charging and discharging. Q_N is the rated capacity, η is the Coulomb efficiency and this paper selects as 0.98. To reduce the dimension of the matrix calculation, note $E_k = U_{OC_k} + H_k$, $R_{0,charge}$ and $R_{0,discharge}$ will be selected based on the direction of the current. SOC can be defined as:

$$SOC(t) = SOC_0 + \frac{\eta \int_0^t I(t)dt}{Q_{\mathrm{N}}} \tag{6}$$

According to Eq. (3), Eq. (7) can be obtained.

$$\begin{bmatrix} \dfrac{\mathrm{d}^{\alpha}}{dt^{\alpha}}U_1 \\ \dfrac{\mathrm{d}^{\beta}}{dt^{\beta}}U_2 \\ \dfrac{\mathrm{d}}{dt}SOC \end{bmatrix} = \begin{bmatrix} -\dfrac{1}{R_1 C_1} & 0 & 0 \\ 0 & -\dfrac{1}{R_2 C_2} & 0 \\ 0 & 0 & 0 \end{bmatrix} \begin{bmatrix} U_1 \\ U_2 \\ 0 \end{bmatrix} + \begin{bmatrix} \dfrac{1}{C_1} \\ \dfrac{1}{C_2} \\ \dfrac{\eta}{Q_N} \end{bmatrix} I \tag{7}$$

$$U = \begin{bmatrix} -1 & -1 \end{bmatrix} \begin{bmatrix} U_1 \\ U_2 \end{bmatrix} - IR_0 + E \tag{8}$$

According to the G-L differential definition, the discrete expression of Eq. (7) can be obtained, as shown in Eq. (9).

$$\begin{bmatrix} U_1(k) \\ U_2(k) \\ SOC(k) \end{bmatrix} = \begin{bmatrix} -\frac{T^\alpha}{R_1 C_1} & 0 & 0 \\ 0 & -\frac{T^\beta}{R_2 C_2} & 0 \\ 0 & 0 & 1 \end{bmatrix} \begin{bmatrix} U_1(k-1) \\ U_2(k-1) \\ SOC(k-1) \end{bmatrix} + \begin{bmatrix} \frac{T^\alpha}{C_1} \\ \frac{T^\beta}{C_2} \\ \frac{T\eta}{Q_N} \end{bmatrix} I(k) - \begin{bmatrix} \lim_{T\to 0} T^{-\alpha} \sum_{j=0}^{L} (-1)^j \binom{\alpha}{j} U_1(k-j) \\ \lim_{T\to 0} T^{-\beta} \sum_{j=0}^{L} (-1)^j \binom{\beta}{j} U_2(k-j) \\ 0 \end{bmatrix} \tag{9}$$

The state space equation of the FH-ECM can be obtained, as shown in Eq. (10).

$$\begin{cases} x_k = A_{k-1} x_{k-1} + B_{k-1} I_{k-1} - \sum_{j=1}^{L} F_j x_{k-j} + w_{k-1} \\ U_k = C_k x_k - I_k R_0 + E_k + v_k \end{cases} \tag{10}$$

Where $A_{k-1} = diag\left\{ -\frac{T^\alpha}{R_1 C_1}, -\frac{T^\beta}{R_2 C_2}, 1 \right\}$, $B_{k-1} = \left[\frac{T^\alpha}{C_1}, \frac{T^\beta}{C_2}, -\frac{T\eta}{Q_N} \right]^T$, $C_k = \left[-1, -1, 0 \right]$. the state variable $x_k = \left[U_1(k), U_2(k), SOC(k) \right]^T$, $F_j = diag\left\{ (-1)^j \binom{\alpha}{j}, (-1)^j \binom{\beta}{j}, 0 \right\}$, w_k and v_k are mutually independent Gaussian white noise. It can be seen that when estimating the state at time k, it is necessary to calculate the state of the past k-1 times, which increases the complexity of the algorithm greatly. When estimating the state of time k, only the influence from time k-L to time k is considered by introducing the short memory principle [41]. It is worth noting that when the state time k does not exceed the memory length, the influence of past k-1 states is considered.

2.2. Parameter identification strategy for GA-PSO

When the model is used for state estimation, it is necessary to identify its parameters. The main difference between FOM and ECM is that there are two CPE, so the discretization expressions of U_1 and U_2 need to be deduced. Combining formula 4 and the G-L definition, the expression of U_1 can be obtained, as shown in Eq. (11).

$$d^\alpha U_1(t) = \frac{I_L(t)}{C_1} - \frac{U_1(t)}{R_1 C_1} = d^\alpha U_1(t) = \lim_{T\to 0} \frac{1}{T^\alpha} \sum_{j=0}^{L} (-1)^j \binom{\alpha}{j} U(t - jT) \tag{11}$$

By discretizing Eq. (11), the expression at time k can be obtained:

$$U_1(k) = T^\alpha \left[\frac{I_L(k-1)}{C_1} - \frac{U_1(k-1)}{R_1 C_1} \right] - \sum_{j=1}^{L} (-1)^j \binom{\alpha}{j} U(k-j) \tag{12}$$

Similarly, the expression of U_2 at time k can be obtained. The parameters to be identified for the model include $\theta = \left(R_0, R_1, R_2, C_1, C_2, \alpha, \beta \right)^T$. The optimal search algorithm is suitable for parameter identification of nonlinear

systems. The genetic algorithm (GA) directly operates on the target and has better global optimization ability. However, the local search ability of the GA is poor, and there are some drawbacks, such as "premature", which can not guarantee the algorithm's convergence. The particle swarm optimization (PSO) algorithm differs from GA in that PSO considers both "location" and "speed" information in the evolution process, whereas GA usually only has "location" information. Over the entire evolutionary process, the globally optimal particles provide information to other particles so that all particles can converge to the optimal solution more quickly. However, in the process of PSO optimization, with the loss of particle diversity, PSO may fall into the local optimum. In this paper, the GA-PSO algorithm is proposed to identify model parameters; in each iteration of PSO evolution, particles are crossed and mutated to ensure the diversity of particles in the optimization process and to effectively reduce the risk of falling into the optimal local solution, and the GA-PSO algorithm flow as shown in Fig. 3.

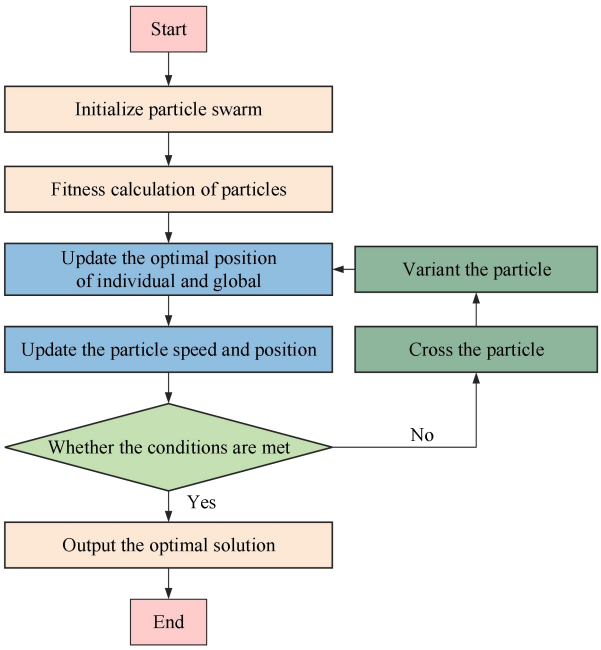

Fig. 3. The GA-PSO algorithm process

Pulse tests are performed at different SOC points, with the minimum RMSE of the terminal voltage as the fitness function, as shown in Eq. (13).

$$\min\left\{\sqrt{\frac{1}{N}\sum_{k=1}^{N}\left[U(k)-\hat{U}(k,\hat{\theta})\right]^2}\right\} \tag{13}$$

2.3. Fractional-order adaptive unscented Kalman filter

In practice, for the highly non-linear system of power batteries, the EKF ignores high-order information during Taylor expansion, which may cause linearization errors and system instability. This paper uses the UKF algorithm to estimate the SOC of batteries. However, the UKF of integer-order systems cannot be applied to fractional-order models, so a fractional-order UKF (FOUKF) algorithm is proposed. Combining the memory characteristics of fractional-order

differentiation and considering the influence of historical information, the problem of SOC estimation based on the FH-ECM is solved. Meanwhile, the FOAUKF estimation strategy is proposed to better adapt to noisy environments.

The discrete state space equation for fractional-order systems is shown in Eq. (14).

$$\begin{cases} d^{\alpha}x(k) = f\left[x\left(k-1\right), \mathrm{u}(k-1)\right] + w(k) \\ y(k) = h\left[x(k), u(k)\right] + v(k) \end{cases} \tag{14}$$

$x(k)$ is the state variable at time k, $u(k)$ is the control variable at time k, and $y(k)$ is the observation variable at time k; $w(k)$ and $v(k)$ represents process noise and observation noise, with variances of $Q(k)$ and $R(k)$. The FOUKF algorithm is constructed as shown in Table 1.

Table 1. Steps for the FOUKF algorithm

Step 1 Calculate the weight coefficient, $\lambda = a^2(n+\kappa) - n$.

$$\begin{cases} W^{(m)}(0) = \dfrac{\lambda}{n+\lambda} \\ W^{(c)}(0) = W^{(m)}(0) + (1-a^2+b) \\ W^{(m)}(i) = W^{(c)}(i) = \dfrac{1}{2(n+\lambda)} \end{cases} \tag{15}$$

Step 2 Initialize state variables and error variance:

$$\begin{cases} \hat{x}^{+}(0) = \mathrm{E}\left[x(0)\right] \\ P^{+}(0) = \mathrm{E}\left\{\left[x(0) - \hat{x}^{+}(0)\right]\left[x(0) - \hat{x}^{+}(0)\right]^{\mathrm{T}}\right\} \end{cases} \tag{16}$$

Step 3 Calculate Sigma sampling point:

$$\begin{aligned} &\chi^{-}(0) = \hat{x}^{+}(k-1) \\ &\chi^{-}(i) = \hat{x}^{+}(k-1) + \left[\sqrt{(n+\lambda)P^{+}(k-1)}\right](i), i = 1, \cdots, n \\ &\chi^{-}(i) = \hat{x}^{+}(k-1) - \left[\sqrt{(n+\lambda)P^{+}(k-1)}\right](i), i = n+1, \cdots, 2n \end{aligned} \tag{17}$$

Step 4 Update status process:

$$d^{\alpha}\hat{x}^{-}(k) = \sum_{i=0}^{2n}\left\{W^{(m)}(i) f\left[\chi^{-}(i), u(k-1)\right]\right\}; \hat{x}^{-}(k) = d^{\alpha}\hat{x}^{-}(k) - \sum_{j=1}^{L}\left[F_j(k-1)\hat{x}^{+}(k-j)\right] \tag{18}$$

Step 5 Update variance process:

$$\begin{aligned} P_{xx} &= \sum_{i=0}^{2n} W^{(c)}(i)\left\{f\left[\chi^{-}(i), u(k-1)\right] - d^{\alpha}\hat{x}^{-}(k)\right\} \bullet \left\{f\left[\chi^{-}(i), u(k-1)\right] - d^{\alpha}\hat{x}^{-}(k)\right\}^{\mathrm{T}} + Q(k-1) \\ P_{\chi x} &= \sum_{i=0}^{2n} W^{(c)}(i)\left[\chi^{-}(i) - \hat{x}^{+}(k-1)\right] \bullet \left\{f\left[\chi^{-}(i), u(k-1)\right] - d^{\alpha}\hat{x}^{-}(k)\right\}^{\mathrm{T}} \\ P_k^{-} &= P_{xx} + \left|F_1(k-1)\right| P_{\chi x} + P_{\chi x}\left|F_1(k-1)\right| + \sum_{j=1}^{L}\left[F_j(k-1)P^{+}(k-j)F_j(k-1)\right] \end{aligned} \tag{19}$$

Step 6 Output posterior estimate:

$$\chi^{+}(i) = f\left[\chi^{-}(i), u(k-1)\right] - \sum_{j=1}^{L}\left[F_j(k-1)\hat{x}^{+}(k-j)\right]; \hat{y}(k) = \sum_{i=0}^{2n}\left\{W^{(m)}(i) h\left[\chi^{+}(i)\right]\right\} \tag{20}$$

Step 7 Update status measurement:

$$P_{yy}=\sum_{i=0}^{2n}W^{(c)}(i)\left\{h\left[\chi^{+}(i)\right]-\hat{y}(k)\right\}\bullet\left\{h\left[\chi^{+}(i)\right]-\hat{y}(k)\right\}^{\mathrm{T}};P_{xy}=\sum_{i=0}^{2n}W^{(c)}(i)\left[\chi^{+}(i)-\hat{x}^{-}(k)\right]\left[\chi^{+}(i)-\hat{x}^{-}(k)\right]^{\mathrm{T}}$$
$$K(k)=P_{xy}\left(P_{yy}\right)^{-1};\hat{x}^{+}(k)=\hat{x}^{-}(k)+K(k)\left[y(k)-\hat{y}(k)\right] \tag{21}$$

Step 8 Update variance measurement:

$$P^{+}(k)=P^{-}(k)+K(k)P_{yy}\left[K(k)\right]^{\mathrm{T}} \tag{22}$$

First, Sigma sample points are constructed, centred on the posterior estimation at the last sampling time, and 2n+1 Sigma points are calculated using the unscented transformation. Secondly, the state and covariance of the system are updated to sum the resulting Sigma points by weight. Considering the influence of historical data, the prior estimate of the state variable is obtained, and then the observed estimate is calculated. Finally, the system state and covariance are updated, the Kalman gain is calculated, the posterior estimate is obtained, and the next iteration is carried out. In step 6, before entering the observation equation, the state needs to be differentiated by fractional order, so the historical value of the memory length needs to be subtracted first.

When using UKF to estimate SOC, $Q(k)$ and $R(k)$ is usually set to a certain value, but in practice, the uncertainty of noise will increase the error of the algorithm in estimating SOC. To better cope with the noise changes in the actual application, an adaptive algorithm is introduced to correct $Q(k)$ and $R(k)$ in real-time, as shown in Eq. (23).

$$\begin{cases}\varepsilon(k)=y(k)-\hat{y}(k)\\ d(k)=(1-l)(1-l^{k+1})^{-1}\\ Q(k)=Q(k-1)+d(k-1)\left[K(k)\varepsilon(k)\varepsilon(k)^{\mathrm{T}}K(k)^{\mathrm{T}}+P^{+}(k)-P^{-}(k)\right]\\ R(k)=R(k-1)+d(k-1)\left[\varepsilon(k)\varepsilon(k)^{\mathrm{T}}-P_{yy}\right]\end{cases} \tag{23}$$

The overall modeling and estimation strategy for this paper is shown in Fig. 4.

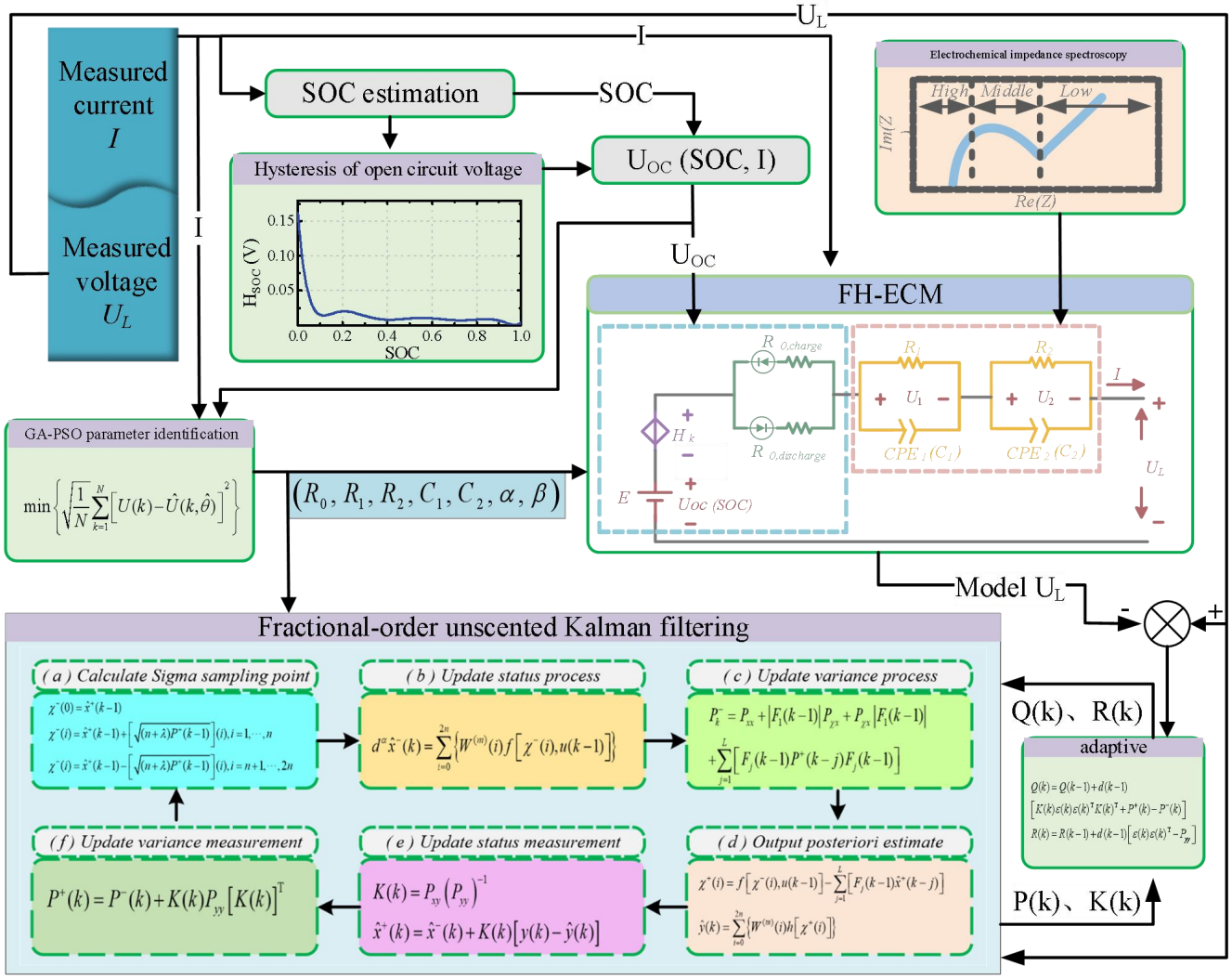

Fig. 4. FH-ECM Modeling and FOAUKF Algorithm framework

3. Experimental analysis

3.1. Experimental platform

To verify the accuracy of the FH-ECM and FOAUKF algorithms, an experimental test platform is built, as shown in Fig. 5. The experimental platform includes lithium-ion batteries, a charge-discharge tester, a temperature control box, and a master computer, the experimental equipment is shown in Fig. 5(a), and the battery sample information is shown in Fig. 5(b).

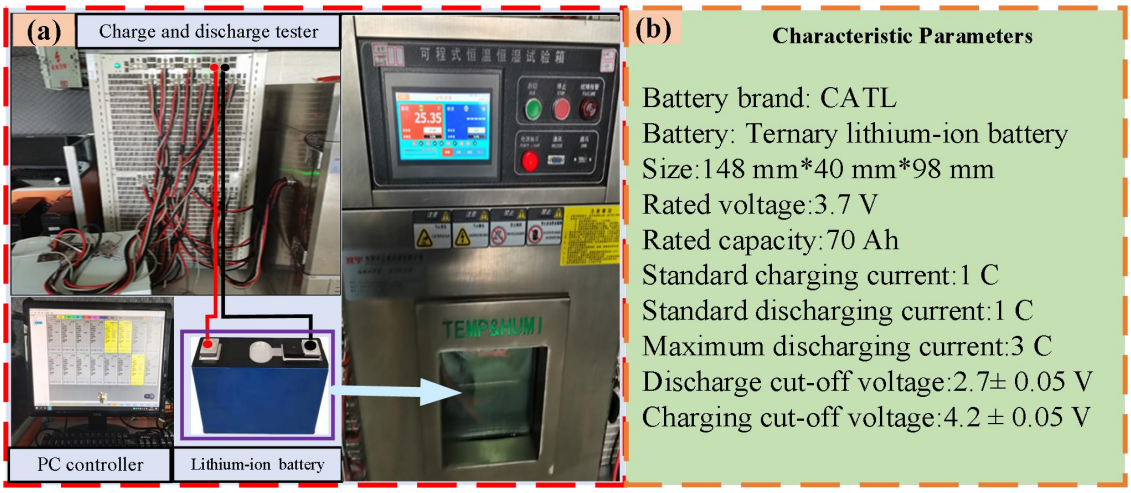

Fig. 5. Battery test platform

3.2. Hysteresis voltage experiments

The accurate model requires an accurate OCV-SOC relationship. In order to obtain the precise relationship between OCV-SOC, this article conducted hysteresis voltage testing on the battery. The battery was discharge-shelving at 0.1C first, then charge-shelving at the same step, as shown in Fig. 6(a). Fig. 6(a) shows that at the same SOC point, OCV at the charging state is more significant than OCV at discharging state, and the difference between them increases significantly at low SOC value, which is related to the increase of chemical reactions inside batteries at the end of discharging.

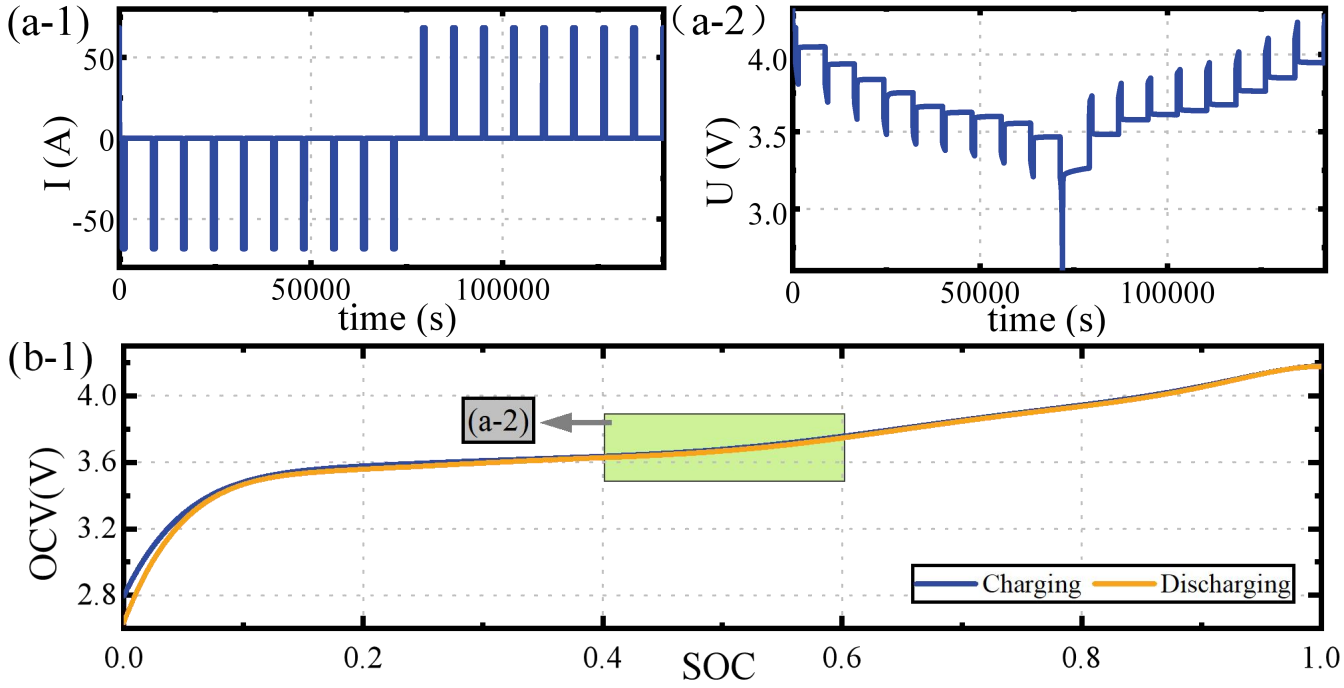

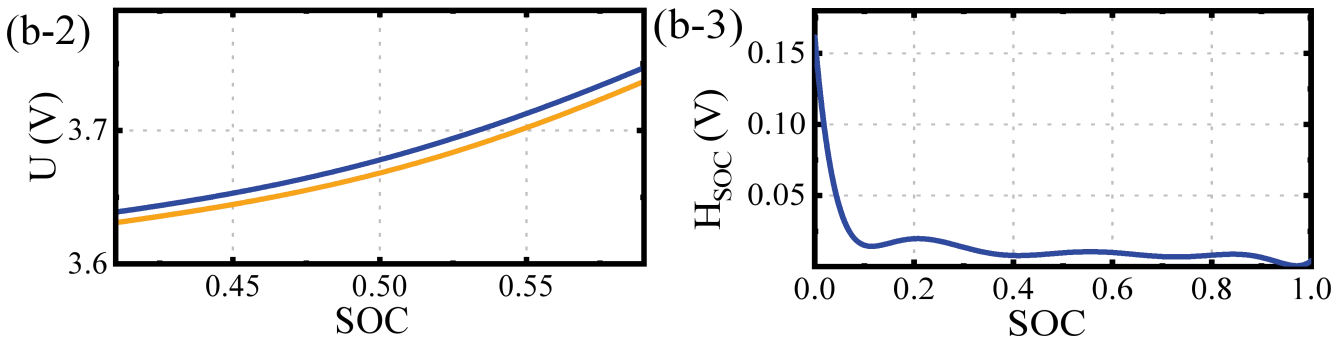

Fig. 6. Hysteresis voltage experiments. (a) Current and voltage in the test. (b) Result of hysteresis voltage test.

OCV-SOC relationship is fitted using the combination model method, and the results are shown in Table 2.

Table 2. Fitting results of OCV-SOC relationship

Charge state:		Discharge state:	
$U_{OC}(SOC) = m_1 + m_2 \ln(SOC) + m_3 \ln(1 - SOC)$		$U_{OC}(SOC) = m_1 + m_2 \ln(SOC) + m_3 \ln(1 - SOC)$	
Results: m1=3.757(3.719, 3.802) m2=0.1253(0.1034, 0.01368) m3=-0.1705(-0.1964, -0.1495)	The goodness of fit: R-square:0.9864 RMSE:0.02358	Results: m1=3.704(3.679, 3.742) m2=0.1237(0.1067, 0.01413) m3=-0.1693(-0.1878, -0.1537)	The goodness of fit: R-square:0.9735 RMSE:0.03648

3.3. HPPC experiments and parameter identification results

The battery was discharged under the Hybrid Pulse Power Cycle (HPPC) test. The current and voltage of the HPPC test are shown in Fig. 7 (a), and the GA-PSO parameter identification results are shown in Fig. 7(b).

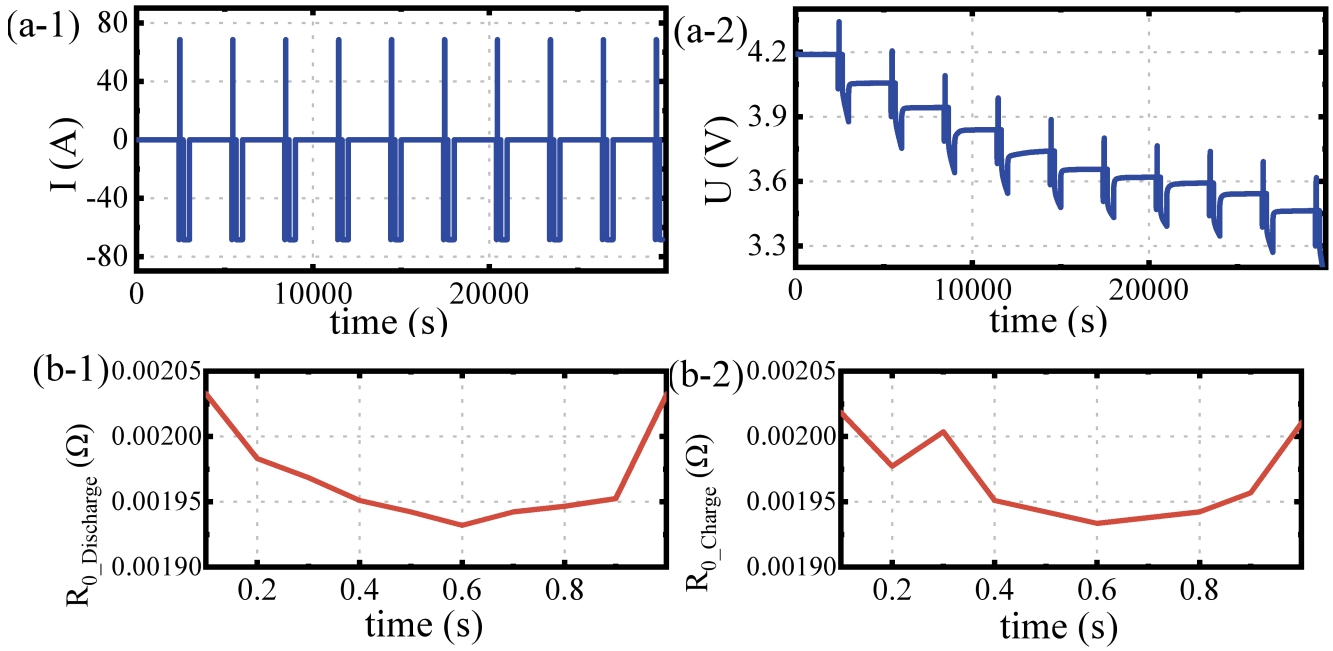

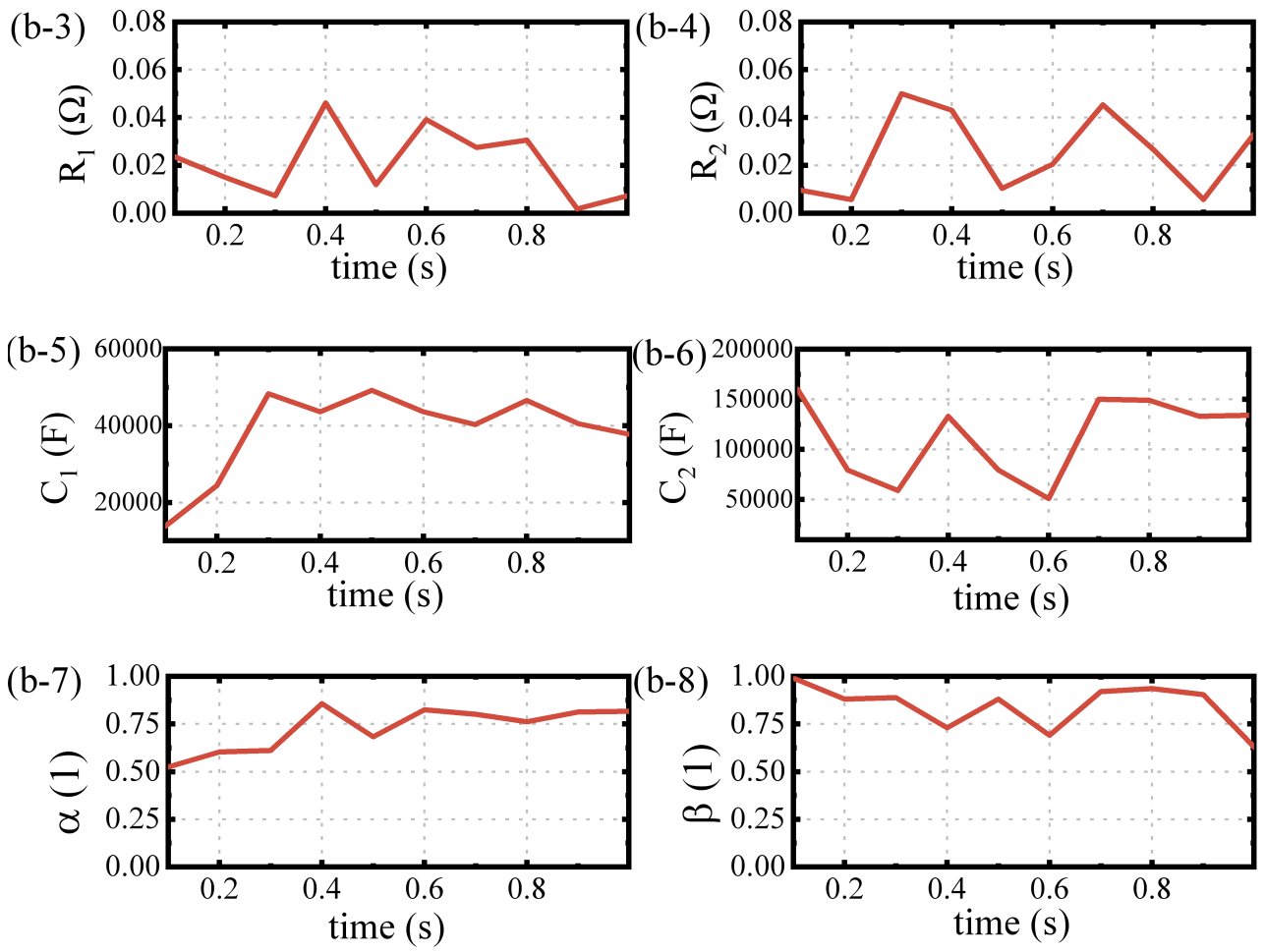

Fig. 7. Hysteresis voltage experiments. (a) Current and voltage under HPPC.

(b) Result of parameter identification results of GA-PSO algorithm.

When the order of CPE is equal to 1, the model is the same as the second-order RC model. However, the identification results indicate that lithium batteries have the characteristics of fractional-order systems. They are comparing the simulation results of terminal voltage between the second-order RC model, FOM, and FH-ECM, as shown in Fig. 8.

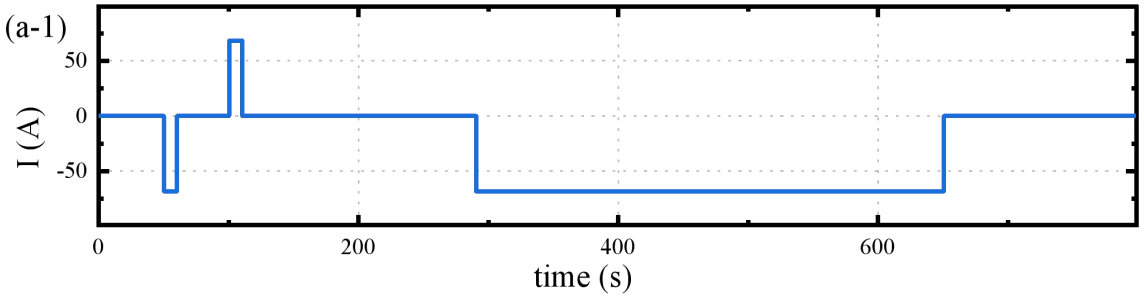

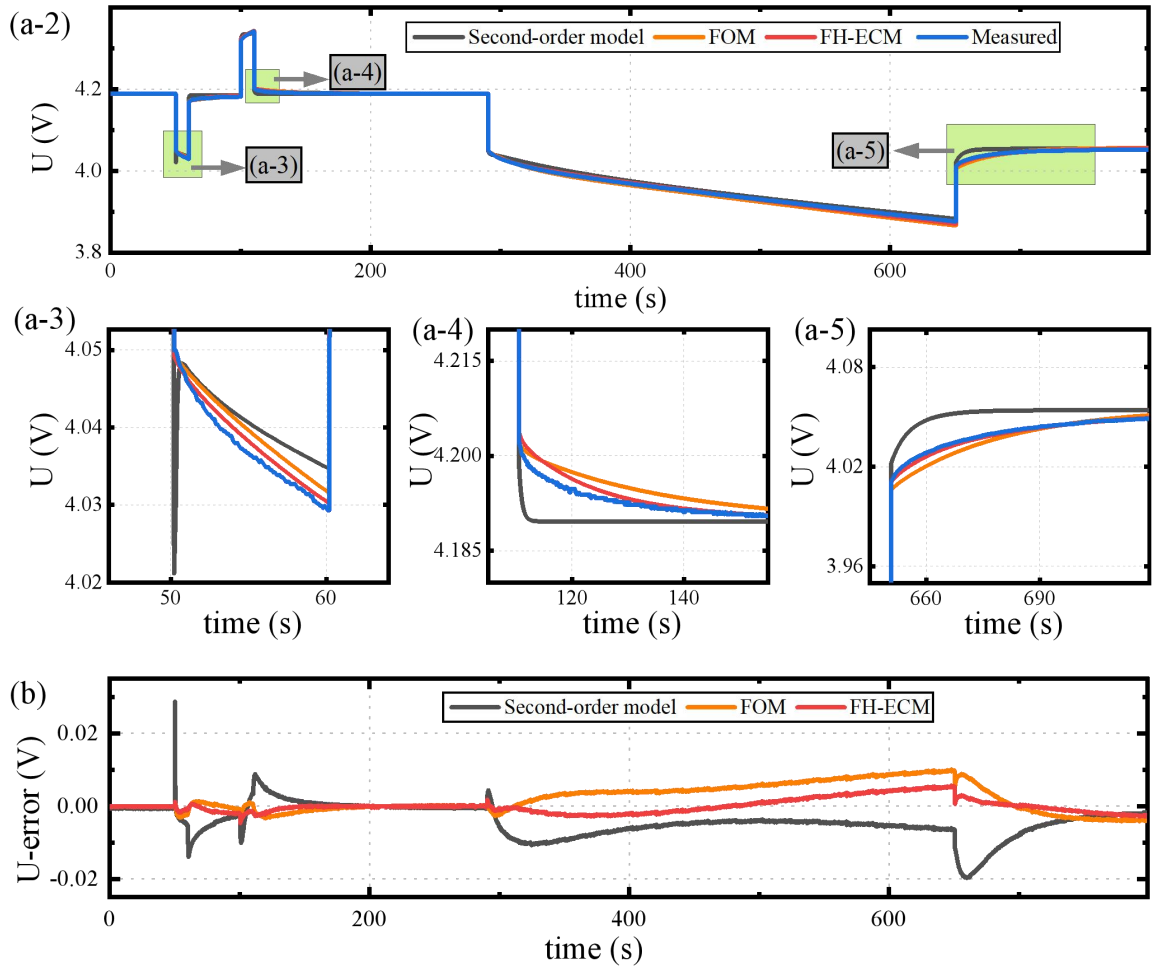

Fig. 8. Hysteresis voltage experiments. (a) Current and voltage in Pulse discharge test.

(b) Error of terminal voltage with different models.

Fig. 8 (a-2) indicates that FH-ECM can better simulate the polarization effect of batteries, with more minor terminal voltage errors and closer proximity to the actual characteristics of batteries.

3.4. Complex working conditions experiments

The discharge mode of the HPPC test is single and cannot reflect the behaviour of the battery under actual working conditions. Therefore, the dynamic stress test (DST) and Beijing bus dynamic stress test (BBDST) were conducted on the battery. Using the SOC calculation value of Coulomb counting method as a reference, and comparing different models and SOC estimation algorithms.

3.4.1. DST working conditions experiments

DST experiments were performed after the batteries were fully charged in the constant current and voltage. The DST test results are shown in Fig. 9. Fig. 9 (a-1) is the current of the DST; Fig. 9 (a-2) is the terminal voltage measurement and model value of the DST; Fig. 9 (a-3), (a-4), and(a-5) is the local amplification diagram of (a-2); Fig. 9(b) is the terminal voltage error of the model.

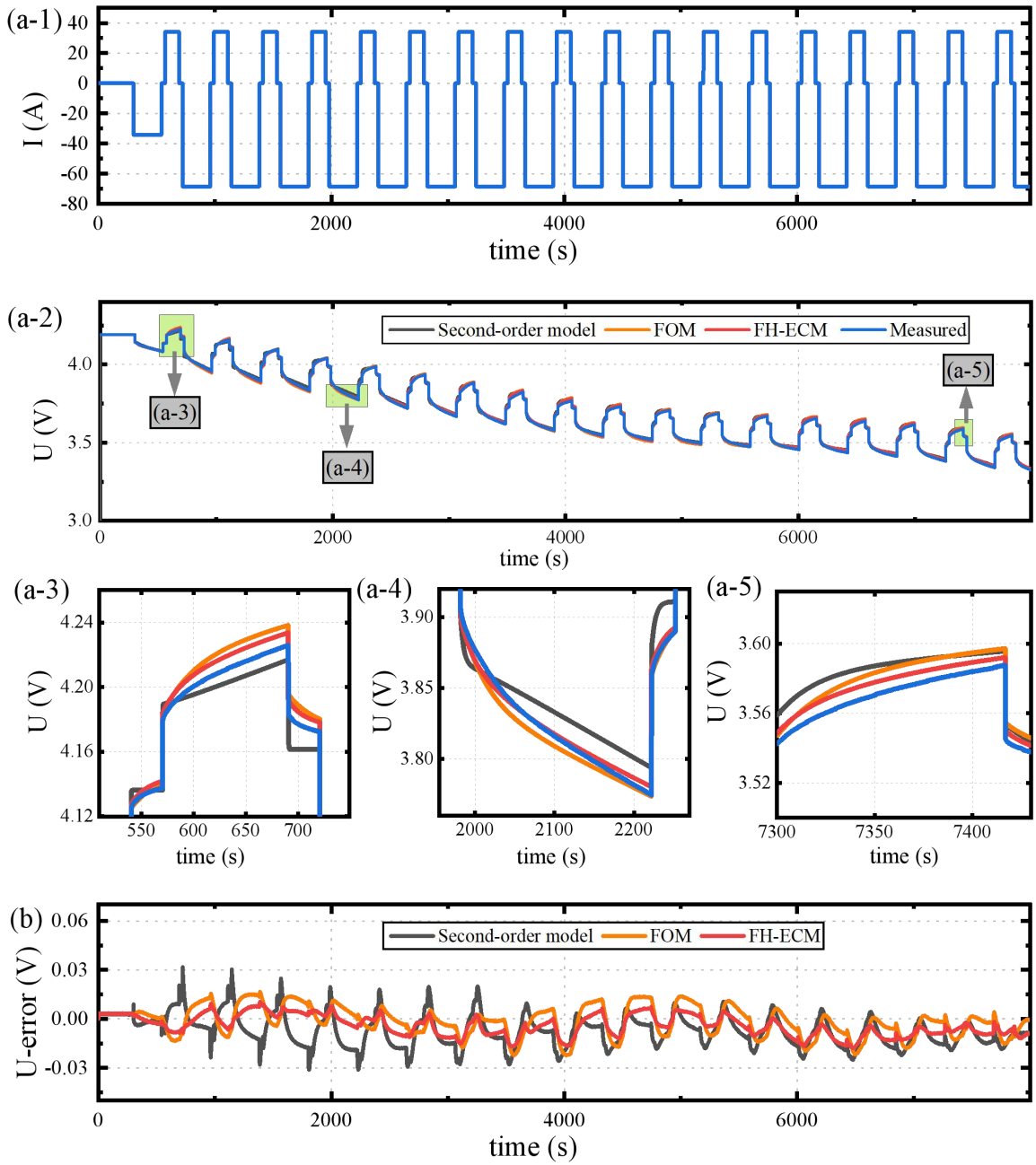

Fig. 9. Model results in DST condition. (a) Current and voltage in DST condition.

(b) Error of terminal voltage with different models.

Fig. 9 (a-2) shows that the second-order RC model and FOM can simulate general voltage changes when simulating the batteries' polarisation effect. However, it has a greater error compared to the FH-ECM. Fig. 9(b) shows that under DST conditions, the areas with significant errors mainly manifest during battery charging or discharging. The maximum error of the second-order RC model exceeds 0.03V and has significant fluctuations, while the error of the FH-ECM generally remains within 0.015V and has minimal fluctuations.

The initial SOC value is deliberately set to 0.8, and the results of different algorithms are compared. Fig. 10 (a-1) is the estimated value and reference value of SOC in DST condition, Fig. 10 (a-2), (a-3), and(a-4) is the local amplification diagram of (a-1), and Fig. 10 (b) is the error of SOC estimation.

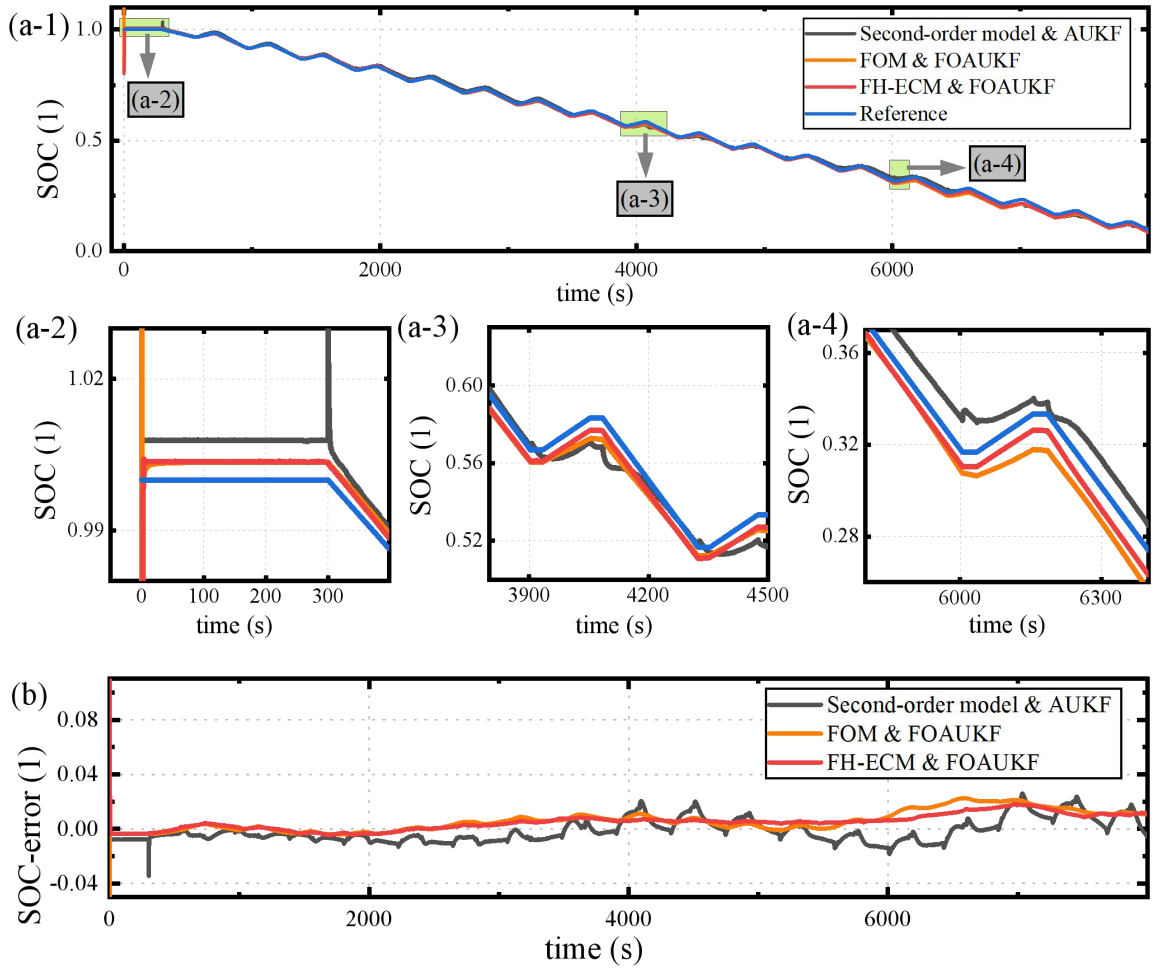

Fig. 10. SOC results in DST condition. (a) estimated value and reference value of SOC in DST condition.

(b) Error of SOC with different algorithms.

Fig. 10 (a-2) shows that FOAUKF and AUKF can quickly converge to the actual SOC value when interference occurs, but FOAUKF has more minor error fluctuations after convergence. Fig. 10 (a-4) shows that FOAUKF can better approximate the changes in SOC at the moment of battery charging or discharging. Fig. 10 (b) shows that the SOC estimation errors of FOAUKF and AUKF in the DST condition are less than 5%, and FOAUKF is more stable with smaller MAXE and RMSE.

3.4.2. BBDST working conditions experiments

Compared to the DST condition, the BBDST condition has a smaller range of changes in battery current and voltage, but the frequency of changes increases significantly. The BBDST test results are shown in Fig. 11. Fig. 11 (a-1) is the two-cycle of current in the BBDST condition, and Fig. 11 (a-2) is the terminal voltage measurement and model value of the BBDST, Fig. 11 (a-3), (a-4), and(a-5) is the local amplification diagram of (a-2). Fig. 11 (b) is the terminal voltage error of the model.

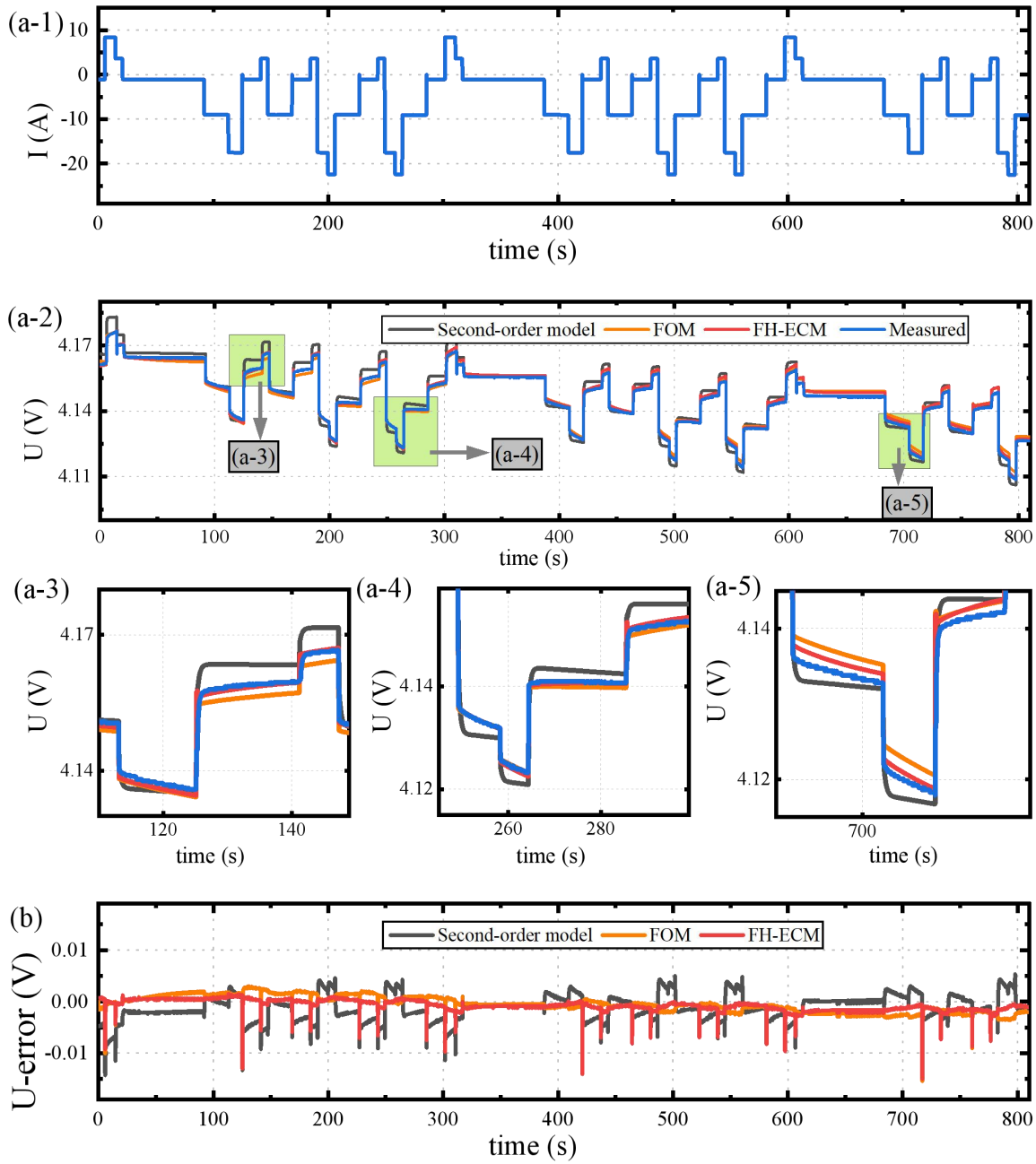

Fig. 11. Model results in BBDST condition. (a) two-cycle of current and voltage in BBDST condition.

(b) Error of terminal voltage with different models.

FH-ECM can better simulate the battery's terminal voltage in high-frequency changing working conditions, and the maximum error does not exceed 0.02V. The initial SOC value is deliberately set to 0.8, and compare the results of different algorithms in the BBDST condition. Fig. 12 (a-1) is the estimated value and reference value of SOC in BBDST condition, Fig. 12 (a-2), (a-3), and(a-4) is the local amplification diagram of (a-1), and Fig. 12 (b) is the error of SOC estimation.

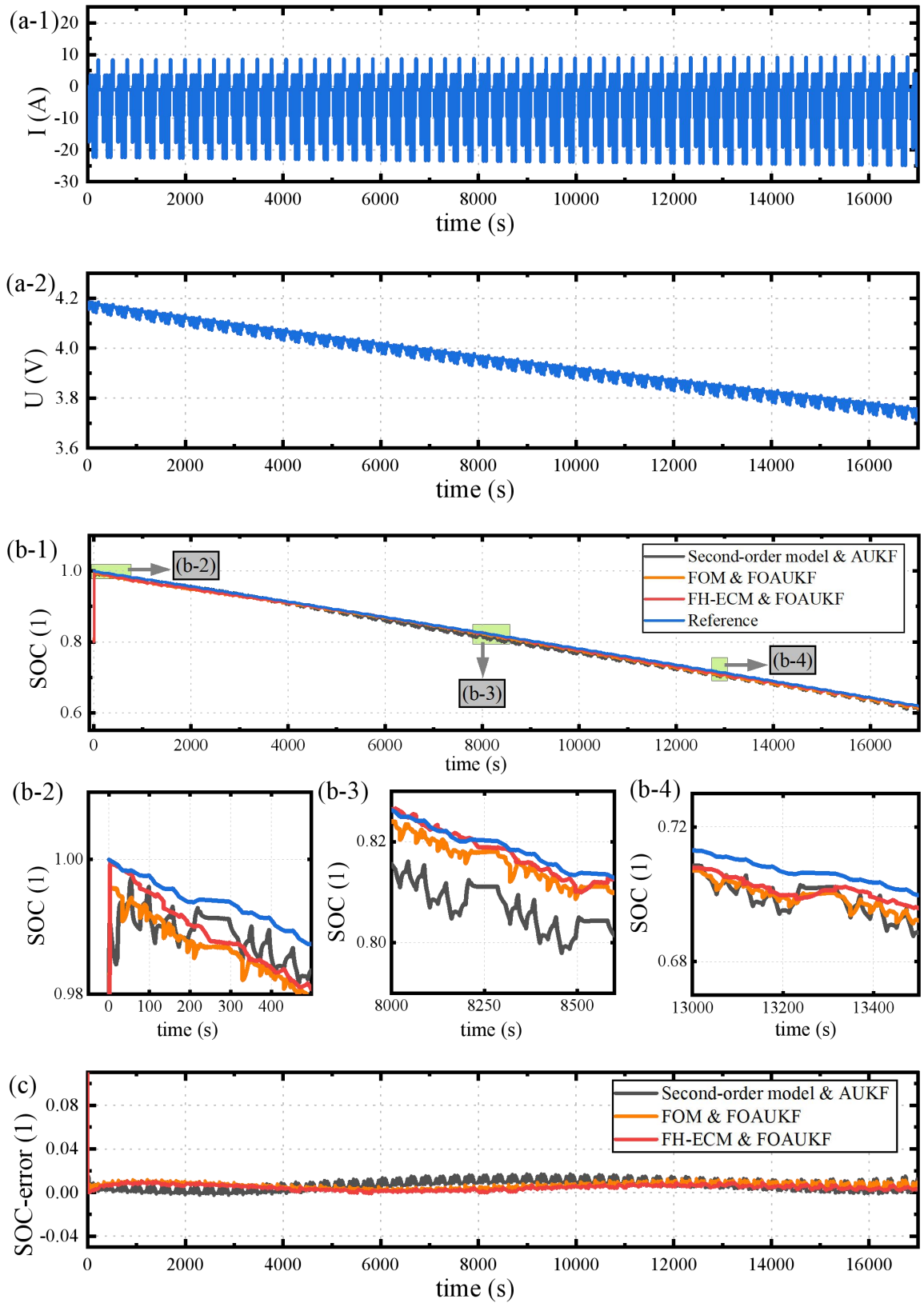

Fig. 12. SOC results in BBDST condition. (a) current and voltage in BBDST condition.
(b) estimated value and reference value of SOC in BBDST condition.
(c) Error of SOC with different algorithms.

Fig. 12 (a-2) shows that FOAUKF can converge more quickly to the actual value with more minor error fluctuations when there are significant fluctuations in SOC values. After the above experiments, it can be concluded that FH-ECM has higher terminal voltage accuracy than the second-order RC model and FOM, and FOAUKF is more stable

in estimating SOC. Fig. 13 (a) shows the RMSE of terminal voltage for different models under different working conditions; Fig. 13 (b) shows the RMSE of SOC for different models under different working conditions.

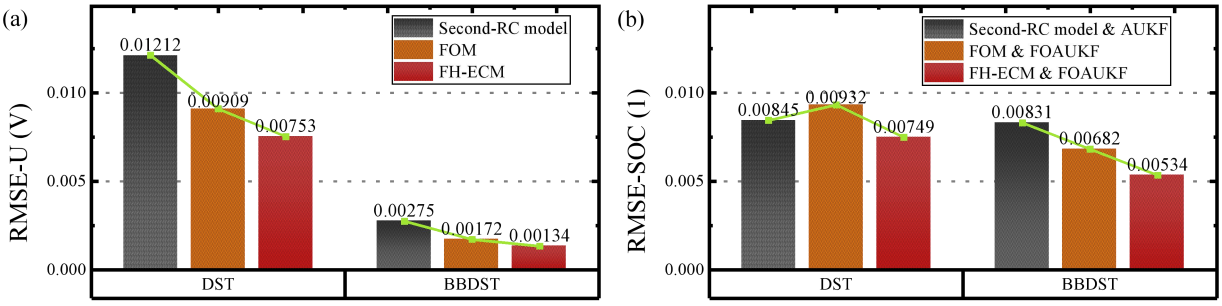

Fig. 13. RMSE of model terminal voltage and SOC estimation.
(a) RMSE of the model terminal voltage in DST&BBDST condition.
(b) RMSE of the model terminal voltage in DST&BBDST condition.

3.5. Comparison of the proposed methods with other existing methods

Comparing FH-ECM with other existing models makes it possible to verify that the model and algorithm are feasible and superior, as shown in Table 3. Include the PNGV model; Thevenin model; Second-order RC model; Fractional-order model. Model reference adaptive system identifies OCV (MRAS & OCV); Weighted multi-innovation cubature Kalman filter (WMICKF); Wiener & EKF; Adaptive central difference Kalman filter (ACDKF). Urban dynamometer driving schedule (UDDS); New Europe Driving Cycle (NEDC).

In Table 3, the model accuracy and SOC estimation accuracy are analyzed comprehensively. FH-ECM and FOAUKF algorithm have good terminal voltage and SOC estimation accuracy. In BBDST condition, the RMSE of end voltage is 0.0013V and the RMSE of SOC is 0.53%. Compared with existing models and methods, it has obvious advantages.

Table 3. Critical performance review of the FH-ECM with other existing SOC methods

Model	Methods	Battery	Verification	Error of terminal voltage	Error of SOC
PNGV	MRAS & OCV [12]	lithium titanate battery 20Ah	HPPC	RMSE：0.0048V	Average error：-1%
Thevenin	WMICKF [14]	LiFePO4 lithium-ion battery 50Ah	UDDS		RMSE：0. 39%
second-order ECM	Wiener & EKF [20]	NMC-based lithium-ion battery 3.4Ah	UDDS	RMSE：0.0107V	RMSE：0. 93%
Fractional-order model	ACDKF [26]	NMC-based lithium-ion battery 94Ah	DST NEDC	RMSE(DST)：0.0070V RMSE(NEDC)：0.0085V	RMSE(DST)：0. 47% RMSE(NEDC)：0.52%
Proposed FH-ECM	FOAUKF	Ternary lithium-ion battery 70Ah	HPPC DST BBDST	RMSE(HPPC)：0.0020V RMSE(DST)：0.0075V RMSE(BBDST)：0.0013V	RMSE(DST)：0. 74% RMSE(BBDST：0. 53%

4. Conclusion

To simulate the actual characteristics of lithium-ion batteries and restore batteries' dynamic response under complex working conditions. Firstly, a high-precision FH-ECM was established based on the second-order RC model, introducing

fractional order theory while considering the influence of the hysteresis effect. Then, the genetic algorithm is introduced to improve the particle swarm optimization algorithm, and the GA-PSO algorithm is used to identify FH-ECM parameters. Thirdly, the FOAUKF algorithm is proposed to estimate the SOC of lithium-ion batteries. Finally, the feasibility of the model and algorithm is verified under Dynamic working conditions. Under the dynamic stress test (DST) condition, the accuracy of model terminal voltage has been improved by 37.83%, and the error of SOC estimation has been reduced by 11.28%. Under the Beijing bus dynamic stress test (BBDST) condition, the model terminal voltage accuracy improved by 51.44%, the RMSE of end voltage was 0.0013V, and the SOC estimation error was reduced by 35.71%. This work confirms the scientific validity of the fractional-order theory in modelling lithium batteries and provides ideas for subsequent modelling.

Acknowledgments

The work is supported by the National Natural Science Foundation of China (No. 62173281, 61801407), Supported by Sichuan Science and Technology Program (No. 2023NSFSC1436), and Fund of Robot Technology Used for Special Environment Key Laboratory of Sichuan Province (No. 18kftk03).

References

[1] Wang, G., et al., A comprehensive review of research works based on evolutionary game theory for sustainable energy development. Energy Reports, 2022. 8: p. 114-136.

[2] Liu, K.L., et al., Towards Long Lifetime Battery: AI-Based Manufacturing and Management. IEEE-CAA Journal of Automatica Sinica, 2022. 9(7): p. 1139-1165.

[3] Viswanathan, V., et al., The challenges and opportunities of battery-powered flight. Nature, 2022. 601(7894): p. 519-525.

[4] Wang, Y.J., et al., A comprehensive review of battery modeling and state estimation approaches for advanced battery management systems. Renewable & Sustainable Energy Reviews, 2020. 131.

[5] Liu, W., T. Placke, and K.T. Chau, Overview of batteries and battery management for electric vehicles. Energy Reports, 2022. 8: p. 4058-4084.

[6] Zhou, L., et al., State Estimation Models of Lithium-Ion Batteries for Battery Management System: Status, Challenges, and Future Trends. Batteries-Basel, 2023. 9(2).

[7] Choi, W., et al., Modeling and Applications of Electrochemical Impedance Spectroscopy (EIS) for Lithium-ion Batteries. Journal of Electrochemical Science and Technology, 2020. 11(1).

[8] Ng, M.F., et al., Predicting the state of charge and health of batteries using data-driven machine learning. Nature Machine Intelligence, 2020. 2(3): p. 161-170.

[9] Li, Y., et al., Adaptive Ensemble-Based Electrochemical-Thermal Degradation State Estimation of Lithium-Ion Batteries. IEEE Transactions on Industrial Electronics, 2022. 69(7): p. 6984-6996.

[10] Wu, L.X., et al., Low-complexity state of charge and anode potential prediction for lithium-ion batteries using a simplified electrochemical model-based observer under variable load condition. International Journal of Energy Research, 2022. 46(9): p. 11834-11848.

[11] Lipu, M.S.H., et al., Intelligent SOX Estimation for Automotive Battery Management Systems: State-of-the-Art Deep Learning Approaches, Open Issues, and Future Research Opportunities. Energies, 2023. 16(1).

[12] Kong, D.P., S.H. Wang, and P. Ping, A novel parameter adaptive method for state of charge estimation of aged

lithium batteries. Journal of Energy Storage, 2021. 44.
[13] Lin, P., et al., Real-time identification of partnership for a new generation of vehicles battery model parameters based on the model reference adaptive system. International Journal of Energy Research, 2021. 45(6): p. 9351-9368.
[14] Fu, S.Y., et al., State of charge estimation of lithium-ion phosphate battery based on weighted multi-innovation cubature Kalman filter. Journal of Energy Storage, 2022. 50.
[15] Hossain, M., M.E. Haque, and M.T. Arif, Online Model Parameter and State of Charge Estimation of Li-Ion Battery Using Unscented Kalman Filter Considering Effects of Temperatures and C-Rates. IEEE Transactions on Energy Conversion, 2022. 37(4): p. 2498-2511.
[16] Chen, Z., et al., State-of-charge estimation of lithium-ion batteries based on improved H infinity filter algorithm and its novel equalization method. Journal of Cleaner Production, 2021. 290.
[17] Yang, F.F., et al., State-of-charge estimation of lithium-ion batteries using LSTM and UKF. Energy, 2020. 201.
[18] Shi, H., et al., On-line adaptive asynchronous parameter identification of lumped electrical characteristic model for vehicle lithium-ion battery considering multi-time scale effects. Journal of Power Sources, 2022. 517.
[19] Tran, M.K., et al., A comprehensive equivalent circuit model for lithium-ion batteries, incorporating the effects of state of health, state of charge, and temperature on model parameters. Journal of Energy Storage, 2021. 43.
[20] Naseri, F., et al., An Enhanced Equivalent Circuit Model With Real-Time Parameter Identification for Battery State-of-Charge Estimation. IEEE Transactions on Industrial Electronics, 2022. 69(4): p. 3743-3751.
[21] Xu, Y.H., et al., Online identification of battery model parameters and joint state of charge and state of health estimation using dual particle filter algorithms. International Journal of Energy Research, 2022. 46(14): p. 19615-19652.
[22] Wang, S.L., et al., An improved feedforward-long short-term memory modeling method for the whole-life-cycle state of charge prediction of lithium-ion batteries considering current-voltage-temperature variation. Energy, 2022. 254.
[23] Feng, H.L., Z.F. Wang, and F.J. Zhang, H infinity-Adaptive H infinity Algorithm-Based State of Charge Estimation Considering the Hysteresis Effect for Lithium Polymer Battery. Frontiers in Energy Research, 2021. 9.
[24] Muresan, C.I., et al., A Review of Recent Advances in Fractional-Order Sensing and Filtering Techniques. Sensors, 2021. 21(17).
[25] Wang, Z. and J.T. Fei, Fractional-Order Terminal Sliding-Mode Control Using Self-Evolving Recurrent Chebyshev Fuzzy Neural Network for MEMS Gyroscope. IEEE Transactions on Fuzzy Systems, 2022. 30(7): p. 2747-2758.
[26] Abu-Shady, M. and M.K.A. Kaabar, A Novel Computational Tool for the Fractional-Order Special Functions Arising from Modeling Scientific Phenomena via Abu-Shady-Kaabar Fractional Derivative. Computational and Mathematical Methods in Medicine, 2022. 2022.
[27] He, L., et al., An adaptive central difference Kalman filter approach for state of charge estimation by fractional order model of lithium-ion battery. Energy, 2022. 244.
[28] Zhou, S.D., et al., Adaptive model parameter identification for lithium-ion batteries based on improved coupling hybrid adaptive particle swarm optimization- simulated annealing method. Journal of Power Sources, 2021. 482.
[29] Zou, C., et al., A review of fractional-order techniques applied to lithium-ion batteries, lead-acid batteries, and supercapacitors. Journal of Power Sources, 2018. 390: p. 286-296.
[30] Xiao, R.X., et al., Comparisons of Modeling and State of Charge Estimation for Lithium-Ion Battery Based on Fractional Order and Integral Order Methods. Energies, 2016. 9(3).
[31] Guo, D.X., et al., Physics-based fractional-order model with simplified solid phase diffusion of lithium-ion battery. Journal of Energy Storage, 2020. 30.
[32] Wang, Y., et al., A fractional-order model-based state estimation approach for lithium-ion battery and ultra-capacitor hybrid power source system considering load trajectory. Journal of Power Sources, 2020. 449.
[33] Li, D.Z., et al., Temperature prediction of lithium-ion batteries based on electrochemical impedance spectrum: A review. International Journal of Energy Research, 2022. 46(8): p. 10372-10388.

[34] Ye, L.H., et al., Co-estimation of lithium-ion battery state-of-charge and state-of-health based on fractional-order model. Journal of Energy Storage, 2023. 65.

[35] Guo, R.H. and W.X. Shen, Lithium-Ion Battery State of Charge and State of Power Estimation Based on a Partial-Adaptive Fractional-Order Model in Electric Vehicles. IEEE Transactions on Industrial Electronics, 2023. 70(10): p. 10123-10133.

[36] Xing, L.K., et al., State-of-charge estimation for Lithium-Ion batteries using Kalman filters based on fractional-order models. Connection Science, 2022. 34(1): p. 162-184.

[37] Solomon, O.O., et al., State of charge estimation of Lithium-ion battery using an improved fractional-order extended Kalman filter. Journal of Energy Storage, 2022. 49.

[38] Sadli, I., et al., Contributions of fractional differentiation to the modelling of electric double layer capacitance. Energy Conversion and Management, 2010. 51(12): p. 2993-2999.

[39] Lee, J.-S.M., et al., Controlling electric double-layer capacitance and pseudocapacitance in heteroatom-doped carbons derived from hypercrosslinked microporous polymers. Nano Energy, 2018. 46: p. 277-289.

[40] Plett, G.L., Extended Kalman filtering for battery management systems of LiPB-based HEV battery packs. Journal of Power Sources, 2004. 134(2): p. 277-292.

[41] Tanekou, G.B., et al., Complex dynamics in the two spring-block model for earthquakes with fractional viscous damping. European Physical Journal Plus, 2020. 135(7).